

Determining the fate of seeded cells in venous tissue-engineered vascular grafts using serial MRI

Jamie K. Harrington,^{*,1} Halima Chahboune,^{§,1} Jason M. Criscione,[§] Alice Y. Li,^{*} Narutoshi Hibino,^{*} Tai Yi,^{*} Gustavo A. Villalona,^{*} Serge Kobsa,[§] Dane Meijas,^{*} Daniel R. Duncan,^{*} Lesley Devine,[‡] Xenophon Papademetri,^{†,§} Toshiharu Shin'oka,^{*} Tarek M. Fahmy,^{*,§,||} and Christopher K. Breuer^{*,2}

^{*}Interdepartmental Program in Vascular Biology and Therapeutics, [†]Department of Radiology, and [‡]Department of Laboratory Medicine, School of Medicine; [§]Department of Biomedical Engineering, and ^{||}Department of Chemical Engineering, Yale University, New Haven, Connecticut, USA

ABSTRACT A major limitation of tissue engineering research is the lack of noninvasive monitoring techniques for observations of dynamic changes in single tissue-engineered constructs. We use cellular magnetic resonance imaging (MRI) to track the fate of cells seeded onto functional tissue-engineered vascular grafts (TEVGs) through serial imaging. After *in vitro* optimization, murine macrophages were labeled with ultrasmall superparamagnetic iron oxide (USPIO) nanoparticles and seeded onto scaffolds that were surgically implanted as inferior vena cava interposition grafts in SCID/bg mice. Serial MRI showed the transverse relaxation times (T_2) were significantly lower immediately following implantation of USPIO-labeled scaffolds ($T_2=44\pm 6.8$ vs. 71 ± 10.2 ms) but increased rapidly at 2 h to values identical to control implants seeded with unlabeled macrophages ($T_2=63\pm 12$ vs. 63 ± 14 ms). This strongly indicates the rapid loss of seeded cells from the scaffolds, a finding verified using Prussian blue staining for iron containing macrophages on explanted TEVGs. Our results support a novel paradigm where seeded cells are rapidly lost from implanted scaffolds instead of developing into cells of the neovessel, as traditionally thought. Our findings confirm and validate this paradigm shift while demonstrating the first successful application of noninvasive MRI for serial study of cellular-level processes in tissue engineering.—Harrington, J. K., Chahboune, H., Criscione, J. M., Li, A. Y., Hibino, N., Yi, T., Villalona, G. A., Kobsa, S., Meijas, D., Duncan, D. R., Devine, L., Papademetri, X., Shin'oka, T., Fahmy, T. M., Breuer, C. K. Determining the fate of seeded cells in venous tissue engineered vascular grafts using serial MRI. *FASEB J.* 25, 000–000 (2011). www.fasebj.org

Key Words: ultrasmall superparamagnetic iron oxide nanoparticles • cellular magnetic resonance imaging • cell tracking

THE DEVELOPMENT OF autologous tissue-engineered vascular grafts (TEVGs) marks a major advancement in overcoming the critical complications associated with the use of synthetic conduits in surgical repairs of complex congenital heart defects (1–4). The TEVGs possess histological and physiological functions similar

to those of native tissues and were designed specifically for use in congenital heart surgery to take advantage of their growth capacity. While our laboratory has both an arterial and a venous model for evaluating TEVG development (5, 6), we used the inferior vena cava (IVC) interposition model in this study to mimic the use of TEVGs in congenital heart surgery (7–9). The vast majority of congenital heart repairs requiring use of a conduit occur in low-pressure, high-flow systems, such as in a Fontan circulation where the venacaval circulation is shunted directly to the pulmonary circulation *via* an extracardiac conduit (10, 11). The IVC replacement model is a validated model for investigating the use of TEVGs in low-pressure, high-flow systems, such as the Fontan circulation. On the basis of results obtained using this model system, we previously performed the first successful clinical study evaluating the use of TEVGs in humans (4). The late-term follow-up from this study is very promising and supports the continued use of TEVGs in congenital heart repairs (3).

In anticipation of continued clinical use, the work in our laboratory has been focusing on delineating the mechanisms of neovessel development with the goal of creating improved, second-generation TEVGs. One major limitation hindering this research is the paucity of available tools for noninvasive monitoring, allowing for repeated observations of a single tissue-engineered vessel as it undergoes dynamic changes. To date, most *in vivo* experiments designed to study the mechanisms of neotissue development on the molecular and cellular levels have required sacrificing the host animals at each observation point in order for the tissue to be harvested for analysis, and thus precluding the ability to perform longitudinal observations in a single animal (12). Noninvasive longitudinal monitoring is increasingly being looked to as a means of studying the cellular and molecular processes occurring during neotissue development in host organisms. The availability of such

¹ These authors contributed equally to this work.

² Correspondence: 10 Amistad St., Amistad Bldg. Rm. 301 C, Yale University School of Medicine, New Haven, CT 06510, USA. E-mail: christopher.breuer@yale.edu

doi: 10.1096/fj.11-185140

noninvasive methods would accelerate the development of improved tissue-engineered constructs, drastically decrease the number of required subjects and associated costs, as well as open the door to human trials.

While intravital microscopy has recently been used to noninvasively monitor the development of TEVGs through the tracking of fluorescently labeled cells, it is not ideal because of the significant limitation of only being able to image superficial tissue and the inability to penetrate polymer-based constructs used in our tissue engineering model (13). Cellular magnetic resonance imaging (MRI) has been the chosen imaging modality for obtaining deeper insight into the underlying *in vivo* biology of many systems and cellular processes without disturbing the native system dynamics because of its ability to depict tissues with greater spatial resolution than other clinical imaging modalities (14, 15), the capacity for whole-body imaging without ionizing radiation (16–20), and the ability for near-cellular resolution with the aid of targeted contrast agents (21, 22). The most widely used contrast agents for cellular MRI in tissue-engineering applications are dextran-coated superparamagnetic iron oxide nanoparticles (SPIOs). MRI has greater sensitivity for superparamagnetic agents than it does for paramagnetic agents, such as gadolinium, which suffer from an inherently high threshold of detectability (16, 20, 23, 24). In addition, superparamagnetic agents are iron based and therefore benefit from a low level of cellular toxicity. Multiple studies have shown that SPIO particles do not adversely affect cell viability, physiology, differentiation, or migration ability (25, 26).

Several groups have used cellular MRI in the context of investigating cellular seeding techniques and in the visualization of cell-seeding efficiency and distribution (27–30). Many groups have also begun to apply cellular MRI to track the fate of cells seeded onto scaffolds intended for tissue regeneration. Most of these studies have been performed *in vitro* (31, 32), but a few groups have performed *in vivo* proof-of-principle studies (33–35). To our knowledge, there have not been any studies that have utilized cellular MRI to answer questions regarding the process of neotissue development after implantation of functional tissue-engineered constructs. We first applied cellular MR imaging to vascular tissue engineering in a pilot study using human aortic smooth muscle cells (hASMCs) labeled with ultrasmall superparamagnetic iron oxide (USPIO) nanoparticles seeded onto TEVGs and implanted as aortic interposition grafts into mice. The animals were imaged at single time points to reveal that the TEVGs seeded with USPIO-labeled cells appeared darker on T_2 -weighted images than unseeded scaffolds (36). It was concluded that USPIO cell labeling enhanced visualization of the tissue-engineered vascular constructs *in vivo*, opening the possibility of applying MRI to temporally and serially track cells on TEVGs *in vivo* that we report in this study.

In this model, TEVGs are created by the classic tissue-engineering paradigm, whereby cells are seeded onto biodegradable scaffolds that are implanted in the host's vasculature, where they develop into neovessels.

Until recently, the idea that cells within the seeded population gave rise to the cells of the neovessel was the most widely held belief about the mechanism of neovessel development (37, 38). Recently, published work from our laboratory (39, 40) has provided initial evidence against this paradigm using histological and PCR-based cell tracking and demonstrating a complete loss of seeded cells within the TEVGs at 1 wk postimplantation. In addition, Hjortnaes *et al.* (13) have successfully used intravital molecular imaging technology corroborated by immunohistochemistry to monitor the *in vivo* time-dependent cell reduction and replacement of seeded cells by host macrophages in carotid TEVG implants.

In this study, we sought to demonstrate our ability to use MRI to serially track USPIO-labeled macrophages seeded onto our TEVGs after they are implanted as interposition grafts in the IVCs of SCID/bg mice. We wanted to complement and confirm the validity of our prior findings that seeded cells are lost from the implanted scaffolds, using serial, noninvasive magnetic resonance imaging methods in order to show that cellular MRI is an ideal technique to noninvasively monitor TEVG development. To achieve this, RAW 264.7 macrophages were labeled with USPIO through *in vitro* culture in medium containing USPIO. The USPIO-labeled macrophages were seeded onto polyglycolic acid (PGA) scaffolds that were surgically implanted as IVC interposition grafts in SCID/bg mice. Images were then obtained on a horizontal bore scanner to determine the transverse relaxation time (T_2) with serial imaging. The signal intensities were verified using Prussian blue staining for iron-containing macrophages. To our knowledge, this is the first study performed in vascular tissue engineering that utilizes serial MRI of a TEVG in a live-animal model to study neovessel development on a cellular level.

MATERIALS AND METHODS

Biodegradable scaffolds

PGA mesh felts (Concordia Fibers, Coventry, RI, USA) were shaped into tubes by introducing 6.0- × 6.0-mm sections into the inlet of a cylinder with an internal diameter of 1.4 mm. Stainless-steel 21-gauge needles were then introduced into the opposing end to maintain the inner lumen and compress the felt. A 5% (w/v) poly-ε-caprolactone and poly-L-lactide [P(CL/LA); Absorbable Polymers International, Birmingham, AL, USA] in dioxane sealant solution was injected into the inlet of the chamber system and allowed to penetrate the felt. The scaffolds were then frozen at -20°C for 20 min and lyophilized for 24 h. This resulted in PGA-P(CL/LA) scaffolds with an internal diameter of 0.9 mm.

Cell culture

Murine macrophages (RAW 264.7; American Type Culture Collection, Manassas, VA, USA) were cultured in RPMI 1640 medium containing 10% FBS and 1% penicillin/streptomycin (Gibco, Carlsbad, CA, USA). Cells were harvested between passages 3 and 6 for all experiments.

Incubation of macrophages with USPIO nanoparticles

Commercially available USPIO nanoparticles (Molday ION (-); Biophysics Assay Laboratory, Worcester, MA, USA) were supplied in 2-ml sterile sealed serum bottles with a concentration of 10 mg Fe/ml. This stock solution of USPIO nanoparticles was diluted directly with serum-free medium (SFM; RPMI 1640 with 1% v/v penicillin/streptomycin; Gibco) for all experiments. Macrophages were incubated at a USPIO concentration of 2 mg/ml for 36 h in SFM.

Prussian blue staining

Prussian blue staining was performed to detect the presence of intracellular iron. Prior to staining, cells were fixed in 10% neutral buffered formalin (NBF; Sigma-Aldrich, St. Louis, MO, USA) overnight. Potassium ferrocyanate (4% w/v in distilled water) was mixed with a 20% w/v solution of hydrochloric acid right before use. The cells were then exposed to this mixture for 20 min before being washed 3 times with distilled water. Cells were then counterstained with nuclear fast red counterstain (Sigma-Aldrich, St. Louis, MO, USA) at room temperature for 5 min. Macrophages receiving no USPIO served as negative controls, and spleen tissue sections served as positive controls.

Cell metabolism assay

A Cell Titer 96 AQueous nonradioactive cell proliferation assay (Promega, Madison, WI, USA) was performed after USPIO labeling. Following the incubation period, the cells were washed 3 times with PBS, and the assay reagent [tetrazolium compound; 3-(4,5-dimethylthiazol-2-yl)-5-(3-carboxymethoxyphenyl)-2-(4-sulfophenyl)-2H-tetrazolium, inner salt (MTS)] and an electron coupling reagent [phenazine methosulfate (PMS)] were added to the cells at a 1:4 ratio with medium and allowed to incubate for 4 h at 37°C. After 4 h, a 100- μ l aliquot of each sample was added to a clear 96-well plate, and the absorbance at 490 nm was read. The relative cell metabolic activity was determined as the ratio of absorbance from wells incubated with USPIO to the control wells (receiving no USPIO). Experiments were performed in triplicate.

Flow cytometry

After USPIO labeling, 7-aminoactinomycin D (7-AAD) flow cytometry was performed and compared to macrophages receiving no USPIO concentration. Cells were pipetted up and down several times to remove attached cells and to break up clumps and were then passed through a 100- μ m cell strainer and transferred to 5-ml polypropylene tubes (BD Bioscience, San Jose, CA, USA). After centrifugation to pellet cells (200 g for 10 min), cells were resuspended in 100 μ l of staining buffer (PBS with 1% FBS and 0.1% sodium azide). To assess viability, 20 μ l of Viaprobe (BD Bioscience) was added to each tube and incubated on ice for 10 min. Next, 200 μ l of staining buffer was added, and the cells were analyzed on a FACSAria cell sorter (BD Bioscience). Results were analyzed using Flowjo (Tree Star, Ashland, OR, USA). Experiments were performed in triplicate.

Macrophage seeding of polymer scaffolds

Each PGA-P(CL/LA) scaffold was trimmed to 4 mm in length and sterilized *via* incubation at 20°C under UV light in sterile PBS. Scaffolds were washed in sterile PBS prior to seeding.

Macrophages were trypsinized and collected for seeding in RPMI 1640 medium. Approximately 5×10^6 cells were statically seeded onto each scaffold by directly pipetting the cell suspension into the lumen through both ends. The scaffold was then gently compressed to encourage cell infiltration into the porous walls. This process of pipetting and compression was repeated 3 times at each end of the scaffold. Each seeded scaffold was then allowed to sit for 15 min to allow cell adhesion. A 21-gauge needle was then gently threaded through the lumen of the graft to prevent occlusion *via* cellular ingrowth, and each graft was incubated overnight in 3 ml of RPMI 1640 medium.

Seeding efficiency determination

Various numbers of USPIO-labeled macrophages (1×10^6 , 5×10^6 , 10×10^6 , and 15×10^6) were statically seeded onto biodegradable PGA-P(CL/LA) scaffold constructs. Seeding efficiency was then determined by measuring the DNA content on the scaffolds with the PicoGreen detection assay (Quant-iT™ PicoGreen dsDNA assay kit; Molecular Probes, Eugene, OR, USA) following 24 h incubation. After 24 h incubation, the seeded scaffolds were rinsed 3 times in PBS, placed in 200 μ l of distilled water, and stored at -80°C for a minimum of 24 h. At the time of evaluation, scaffold sections were thawed at 37.8°C . A black 96-well plate was loaded with 50 μ l from each sample. A 30- μ l aliquot of the PicoGreen dye was mixed thoroughly with 6 ml of Tris-EDTA buffer (pH 7.5), and 50 μ l was added to each sample in the 96-well plate. All assays were performed in triplicate. The plate was incubated in the dark at room temperature for 10 min. Fluorescence was measured at 488-nm excitation and 525-nm emission. The number of cells maintained on each scaffold was determined from a standard curve generated from a known quantity of macrophages. A negative control of unseeded scaffold sections was used for comparison.

MRI

All MRI experiments were performed on a 4T Bruker horizontal-bore system (Bruker Bio-Spin, Billerica, MA, USA) with custom-made bird-cage coils. For T_2 -weighted images, a rapid-acquisition relaxation-enhanced (RARE) spin-echo (SE) sequence was used with the following parameters: retention time (T_R)/echo time (T_E) = 3000/20 ms; matrix size = 128×128 ; field of view (FOV) = 32×32 mm; slice thickness = 1 mm; RARE factor = 8. For T_2 maps, the images were acquired using a multispin multiecho (MSME) with the following parameters: T_R/T_E = 3000/18 ms, number of echoes = 8 with T_E spacing = 18 ms; matrix size = 128×128 ; FOV = 32×32 mm; slice thickness = 1 mm. T_2 maps were generated by performing fits of the multiple images to a monoexponential decay on a pixel-by-pixel basis using home-written MatLab (Natick, MA, USA) software. The transverse relaxation rate R_2 ($1/T_2$) was calculated, and the results were fitted to $R_{2 \text{ labeled}} - R_{2 \text{ unlabeled}} = r_2 N$, where r_2 is the relaxivity per cell for Molday ion, and N is the number of cells in a 1-mm slice.

In vitro MRI of cell suspensions

To determine the minimal quantity of detectable cells, decreasing numbers of labeled cells (25×10^6 , 20×10^6 , 15×10^6 , 10×10^6 , 5×10^6 , and 1×10^6), and unlabeled cells were imaged in gelatin phantoms. Labeled cells were fixed in 10% NBF overnight and were then homogeneously suspended in Histogel (Richard-Allan Scientific, Kalamazoo, MI, USA). The known cell numbers were suspended in 500 μ l of PBS using

Corning 96-well polypropylene cluster tubes (Corning, Corning, NY, USA), and then 500 μ l of Histogel was added, pipetting up and down to ensure the cells were homogeneously suspended. Controls consisted of samples without cells and samples with unlabeled cells. The cellular limit of detection was determined by analyzing the T_2 maps of the cellular suspensions. The number of cells in each 1-mm slice of the homogenous cell suspension was determined by calculating the volume of the cylindrical tube used for the MRI (height = 1 mm, radius = 3.5 mm). This number corresponded to a given T_2 value for each sample.

***In vitro* MRI of scaffold suspensions**

Biodegradable scaffolds were seeded with USPIO-labeled macrophages and unlabeled macrophages, as described previously. On d 1 postseeding, the seeded scaffolds were suspended in Histogel in Corning 96-Well polypropylene cluster tubes. As controls, one tube was filled with Histogel, and one contained an unlabeled scaffold.

Surgical implantation of scaffolds

Anesthesia was induced by inhalation of 4% vaporized isoflurane in a mixture of oxygen. During the surgical procedure, isoflurane was maintained in 0.5–1.5% without any clinical signs of pain or changes of macrohemodynamic parameters. On induction of anesthesia, the animals were placed in a supine position. Using an $\times 18$ dissecting microscope (Zeiss, Thornwood, NY, USA), a midline laparotomy was performed, and the abdominal viscera were lateralized to allow visualization of the abdominal aorta. Care was taken to separate the aorta from the vena cava. Proximal and distal vascular control of the vessels was obtained below the renal vessels and above the iliac bifurcation. The open abdominal cavity was bathed in warmed (37°C) heparinized saline (250 U/ml). The native vessel was gently occluded with removable microvascular clamps and then transected. Anastomosis to a caliber-matched TEVG (1-mm diameter) was performed at the infrarenal level of the IVC using interrupted 10-0 monofilament nylon (Sharp Point Lab Sutures, Calgary, AB, Canada). On completion of the distal anastomosis, the midline incision was closed with running 5-0 prolene sutures. After laparotomy closure, animals were monitored during recovery and placed on a warm pad to avoid hypothermia. The animals recovered from surgery and were maintained without the use of any anticoagulation or antiplatelet therapy.

Animal handling was in accordance with Yale University institutional guidelines for the use and care of animals, and the institutional review board approved the experimental procedures.

***In vivo* serial MRI**

Mice with seeded labeled ($n=3$) or seeded unlabeled ($n=3$) scaffold implants underwent *in vivo* imaging. For all *in vivo* imaging, the mice were maintained anesthetized with 1.5% isoflurane applied with a face mask, which allowed free breathing. Respiration was monitored using a balloon taped to the thorax and connected to a pressure transducer. The mice were imaged immediately following surgical implantation of the scaffolds and on postoperative d 7. For a more precise temporal analysis of the increase in T_2 signal, one additional mouse was imaged immediately after the implantation every 30 min for 9 h.

Histological analysis

All infrarenal IVC scaffolds were explanted and fixed in 10% NBF overnight prior to histological embedding with glycolmethacrylate (GMA). GMA-embedded samples were stained with Lee's methylene blue with a nuclear red counterstain. Scaffolds were stained for the presence of intracellular iron with Prussian blue, as described previously.

Cell counting

Two separate sections of each scaffold explant were stained with hematoxylin and eosin (H&E) and Prussian blue and imaged at $\times 400$. Numbers of nuclei were counted in 4 regions of each section and averaged to determine total cellularity. Numbers of cells staining positive for Prussian blue were counted in 4 regions of each section and averaged to determine total number of cells containing USPIO nanoparticles.

Statistical analysis

Statistical differences were analyzed with paired and unpaired Student's *t* tests or ANOVAs. Values of $P < 0.05$ were considered statistically significant.

RESULTS

Macrophage labeling with USPIO and scaffold seeding

Successful *in vitro* USPIO nanoparticle cell labeling of the RAW 264.7 cell line was achieved without affecting cellular metabolic activity or viability by incubating them with a USPIO concentration of 2 mg/ml for 36 h in SFM. After cell labeling, Prussian blue staining, performed to reveal intracellular iron deposits, consistently showed a robust labeling efficiency (Fig. 1A, B). The metabolic activity and cellular viability of labeled macrophages, as measured using the MTS assay and flow cytometry, respectively, were not statistically different from control macrophages (receiving a USPIO concentration of 0 mg/ml; Table 1).

Once robust cell labeling was achieved without affecting cellular metabolism or viability, the static seeding efficiency of the USPIO-labeled macrophages onto our PGA biodegradable polymer scaffolds was determined to be $\sim 8\%$. This is consistent with cell-seeding studies that show a seeding efficiency between 5 and 10%, depending on the cell line being used (30). With this seeding efficiency, 5 million macrophages could be statically seeded onto each scaffold resulting in retention of $\sim 3.8 \times 10^5 \pm 13\%$ cells. Histological sections of the seeded scaffolds showed the macrophages were able to penetrate the pores of the PGA mesh and were able to remain well infiltrated into the walls and attached to the lumens and exteriors of the scaffolds, even after scaffold manipulation (Fig. 1C, D).

***In vitro* MRI analysis**

Labeled macrophages were homogeneously suspended in Histogel in 7 serial dilutions from 25×10^6 to 0

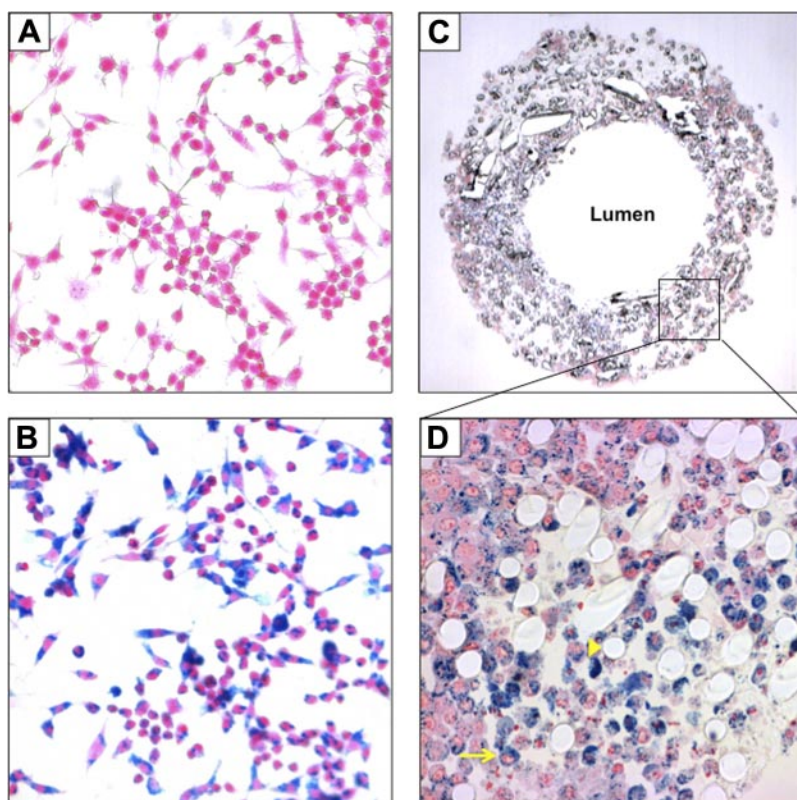


Figure 1. Evaluation of USPIO cell labeling and scaffold cell seeding. Murine macrophages were stained with Prussian blue to identify intracellular iron. *A*) Photomicrograph of unlabeled control macrophages (H&E, $\times 400$). *B*) Photomicrograph of macrophages after USPIO cell labeling (H&E, $\times 400$). *C*) Photomicrograph of USPIO-labeled macrophages statically seeded onto a biodegradable scaffold (Lee's methylene blue, $\times 40$). *D*) Representative section of the seeded scaffold in *C*, showing the PGA scaffold fibers (arrowhead) and the USPIO-labeled macrophages (arrow; Lee's methylene blue, $\times 400$).

cells/ml of Histogel suspension. T_2 -weighted images were then acquired using an SE sequence. USPIO is a T_2 contrast agent that shortens the transverse relaxation time, resulting in a hypodense (dark) signal. T_2 -weighted images (Fig. 2A) showed a gradual decrease of the signal intensity as the number of labeled cells increased in the samples. At very high concentrations of labeled cells (25×10^6 cells/ml), the signal loss was no longer discernable from the background noise. Figure 2B represents the corresponding T_2 maps of the same sample; T_2 values decreased with increasing numbers of labeled cells (Table 2). At very high labeled cell concentrations (25×10^6 cells/ml), the T_2 value could no longer be detected since the value exceeded the measurable threshold given the acquisition parameters' range.

T_2 values were calculated for each 1-mm MRI slice, and on the basis of known cell numbers in each 1-mm MRI slice, the T_2 value was correlated with a given number of USPIO-labeled macrophages. T_2 values ranged from 202 ms for the gelatin phantom without any USPIO-labeled macrophages to 15.4 ms for the

sample with 20×10^6 macrophages (the sample with the highest amount of iron oxide that was still in signal range). Although the T_2 values gradually increased for samples B through E, as the cell numbers decreased from 20×10^6 ($\sim 700,000$ cells/1-mm slice) to 5×10^6 ($\sim 175,000$ cells/1-mm slice), T_2 values were consistently low compared to the gelatin phantom that did not contain any iron oxide, ranging from 15.4 to 48 ms. It was not until the cell numbers decreased to 1×10^6 ($\sim 35,000$ cells/1-mm slice) that the T_2 value showed a significant increase to 140 ms. In other words, sample E is the first concentration of iron oxide in which the signal void (T_2 shortening) begins to become apparent compared to samples F and G (control). On the basis of these T_2 values, the cellular limit of detection was determined to be between 175,000 and 35,000 cells. This detection limit fell well below the macrophage retention number after static seeding ($\sim 3.8 \times 10^5 \pm 13\%$ cells), providing evidence for the feasibility of MRI detection on our biodegradable scaffolds. Figure 2E shows the relationship between R_2 and labeled cell concentration under *in vitro* conditions. R_2 ($1/T_2$) values exhibit a linear correlation with labeled cell concentrations ($R^2=0.97$).

Next, to confirm the potential for cell tracking on a clinically relevant substrate, USPIO-labeled macrophages were seeded onto biodegradable scaffolds for *in vitro* MRI analysis. Three scaffolds were suspended in Histogel for MRI analysis and T_2 mapping, one scaffold seeded with USPIO-labeled macrophages, one scaffold seeded with unlabeled macrophages, and one unseeded scaffold (Fig. 2C, D). The T_2 values for the scaffolds were 26.66, 45.38, and 84.50 ms, respectively

TABLE 1. Cell viability and metabolic activity of USPIO-labeled macrophages

Parameter	n	USPIO concentration (mg/ml)		P
		2	0	
Metabolic activity	6	2.99 ± 0.10	3.22 ± 0.06	0.08
Cellular viability	7	63.58 ± 0.89	62.99 ± 2.37	0.82

Values are expressed as means \pm SE.

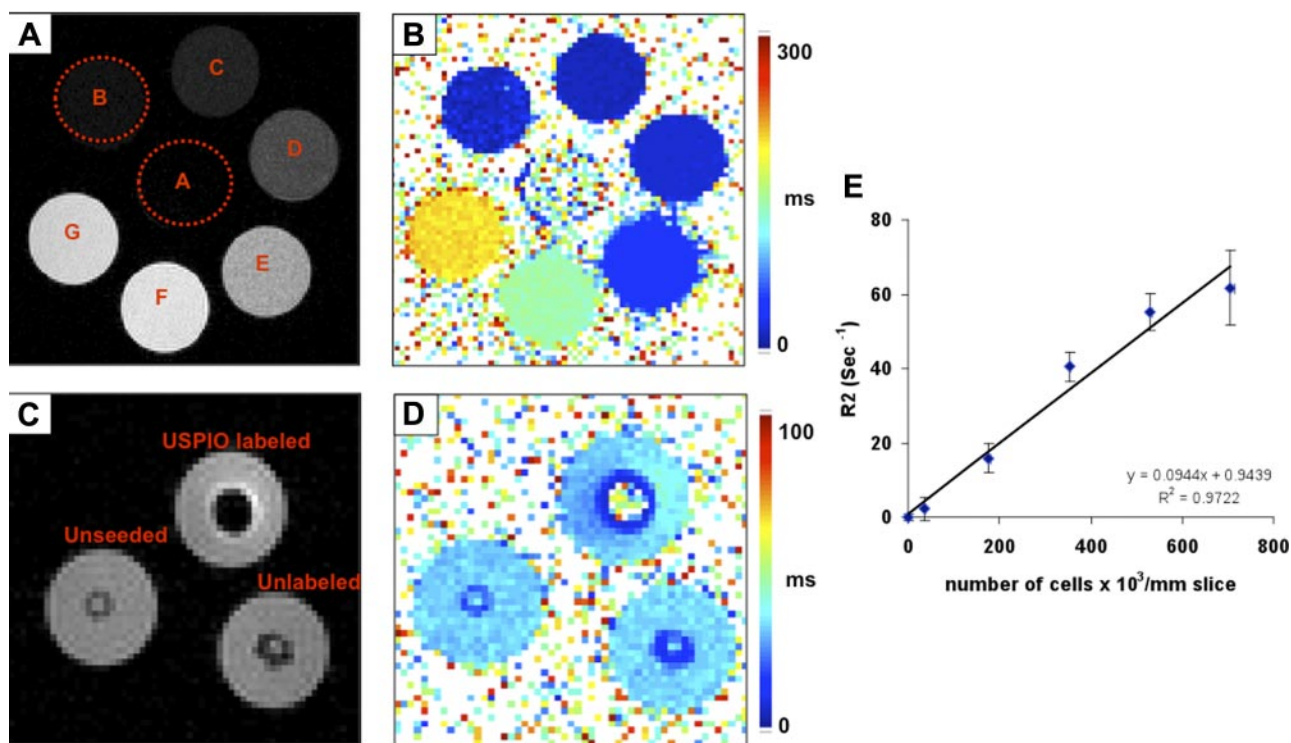


Figure 2. *In vitro* characterization of USPIO-labeled macrophages and seeded scaffolds. *A*) T_2 -weighted image of a gelatin phantom using an array of concentration gradients of USPIO-labeled macrophages. Labeled cells (n): A, 25×10^6 ; B, 20×10^6 ; C, 15×10^6 ; D, 10×10^6 ; E, 5×10^6 ; F, 10^6 ; G, 0. *B*) T_2 mapping of sample in panel A. *C*) *In vitro* T_2 -weighted image of an unlabeled scaffold, an unseeded scaffold, and a USPIO-labeled scaffold suspended in gelatin. *D*) T_2 mapping of sample in panel C. *E*) Relationship between relaxation rate R_2 and labeled cells in gelatin phantoms. The R^2 exhibits significant correlation with labeled cell concentration ($R^2=0.97$).

(**Table 3**). The region of signal void created around the scaffold seeded with labeled macrophages was significantly larger than the void created by the scaffold seeded with unlabeled macrophages or the unseeded scaffold. This confirmed that labeling macrophages with USPIO substantially reduced the MRI signal intensity around the scaffold, making it appear uniformly dark and easily detectable on MRI. Interestingly, the T_2 value for the USPIO-seeded scaffold was 26.66 ms, a number that closely resembles the T_2 value calculated for the USPIO cell suspension containing $\sim 350,000$ cells/1-mm slice (22 ms, sample D). We investigated the effect of background scaffold differences on the relationship between R_2 ($1/T_2$) and labeled cell concentrations. We calculated the R_2 differences (ΔR_2) by subtraction of the R_2 value in the unseeded scaffold from the R_2 value in the

scaffold seeded with labeled cells. The ΔR_2 measured was converted to cell concentration using the standard curve of R_2 against the known labeled cells concentrations (Fig. 2E). The number of labeled cells in the scaffold was estimated to be $\approx 274,000$ cells/mm slice thickness. The number of cells determined using the calibration curve corresponds to the macrophage retention after static seeding, which is $\sim 300,000$ cells; this number was determined by performing a DNA assay after static seeding and overnight incubation. On the basis of this result, we believe that the higher background generated with the scaffold does not significantly affect the correlation between the T_2 and the number of macrophages *in vitro*.

While we are confident in our *in vitro* correlation between USPIO-labeled macrophage cell numbers and relaxivity, we recognize that this correlation will not be the same *in vivo*. It is very difficult to perform exact R_2 ($1/T_2$)-based quantifications *in vivo* using iron oxide, especially in longitudinal studies. *In vivo*, R_2 changes are caused not only by the USPIO-labeled cells, but also by

TABLE 2. *In vitro* T_2 values of USPIO-labeled macrophages

Sample	Labeled cells (n)	Cells in 1-mm slice (N)	T_2 (ms)
A	25×10^6	882,080	Out of range
B	20×10^6	705,664	15.4
C	15×10^6	529,248	16.5
D	10×10^6	352,832	22
E	5×10^6	176,416	48
F	1×10^6 ^a	35,283	140
G	Control ^a	0	202

^aBelow the limit of detection.

TABLE 3. *In vitro* T_2 values of scaffolds seeded with USPIO-labeled macrophages

Scaffold	T_2 (ms)
USPIO labeled	26.66
Non-USPIO labeled	45.38
Unseeded	84.5

motion and susceptibility artifacts caused by respiratory rate, pulse rate, and gut pulsation. However, our *in vitro* data have confirmed our ability to track USPIO-labeled cells *in vitro* on our biodegradable scaffolds in quantities that are well above our macrophage-seeding efficiency.

In vivo serial MRI analysis and cell tracking

For *in vivo* MRI analysis, SCID/beige mice were surgically implanted with TEVGs seeded with USPIO-labeled macrophages ($n=3$) and TEVGs seeded with unlabeled macrophages ($n=3$) as controls. The TEVGs were implanted as infrarenal interposition grafts in the IVCs of the mice. After implantation, RARE T_2 -weighted images were obtained immediately postoperatively ($n=3$) and at 1 wk postimplantation ($n=3$) in all the mice. Representative RARE T_2 -weighted images and their corresponding T_2 maps are shown in **Fig. 3**.

The TEVGs were easily identified retroperitoneally in the infrarenal IVCs of mice, both immediately after implantation and after 1 wk. T_2 values were calculated for the TEVGs seeded with both USPIO-labeled and unlabeled macrophages, as well as for other tissues, including liver, muscle, and fat. In the T_2 -weighted images in **Fig. 3A, B**, it is difficult to see the difference between the control and seeded scaffolds in terms of contrast; both scaffolds created hypointensities in the T_2 -weighted images. However, the seeded scaffold creates a “blooming” hypointensity because of the USPIO inside the cells. The T_2 maps reveal the differences in T_2 values between the two scaffolds. Most of the pixels in the seeded scaffold are represented by a dark blue, which translates to a T_2 value of 20–40 ms. The pixels in the control scaffold are much lighter, the T_2 ranged from 70 to 80 ms. The T_2 values measured in all the tissues outside of the IVC implants were similar in both groups immediately after implantation and at 1 wk postimplantation (**Fig. 4A, B**).

The T_2 maps reveal significantly lower T_2 values in the TEVGs seeded with USPIO-labeled macrophages immediately postoperatively ($T_2=44\pm 6.8$ vs. 71 ± 10.2 ms; **Fig. 4A**). This finding was no longer apparent at 7 d postoperatively ($T_2=63\pm 12$ vs. 63 ± 14 ms). The drop in the T_2 values seen in the TEVGs seeded with USPIO-labeled macrophages verifies that the seeded macrophages were retained on the scaffold after surgical implantation in numbers greater than the MRI cellular limit of detection and that these cells were lost from the scaffold by 1 wk, such that the signal difference was no longer significantly detectable. To gain further insight into the time frame within which the USPIO-seeded macrophages were lost from the scaffold implants, additional mice were serially imaged in 30-min increments immediately after scaffold implantation for up to 9 h. The T_2 values were calculated for each time point and showed a rapidly progressive increase in the T_2 value for the USPIO-seeded scaffold (**Fig. 4C**). The T_2 value increased to control values by 90–120 min after implantation, indicating that the cells are rapidly lost from the implanted TEVG.

Histological analysis

These findings were verified with histology of USPIO-labeled and non-USPIO-labeled TEVG explants immediately after implantation ($T=0$), at 2 h after implantation (after the T_2 value is shown to increase to control levels), and 1 wk after implantation. Explants were sectioned and stained from 4 mice at each time point ($T=0$, $T=2$ h, $T=1$ wk). The scaffold explants were embedded in GMA and stained with Prussian blue to identify intracellular iron deposits. The numbers of cells containing intracellular iron deposits, as well as the total number of cells in each scaffold, were determined at each time point (**Fig. 5**).

There were significantly more Prussian blue-stained

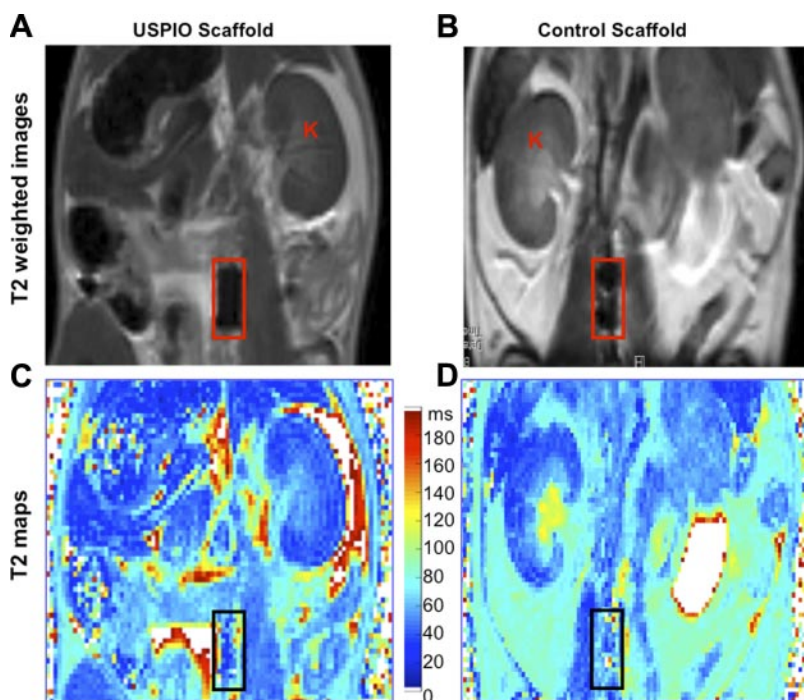


Figure 3. *In vivo* MR imaging of labeled and unlabeled scaffold implants. **A, B**) Representative axial T_2 -weighted RARE images of mice implanted with labeled (**A**) and unlabeled (**B**) seeded scaffolds, illustrating the location of implanted scaffolds (boxes). Kidneys (K) and liver (L) are visible in the images. **C, D**) Corresponding T_2 maps of the same slices, showing T_2 value differences between the labeled (**C**) and unlabeled (**D**) seeded scaffolds.

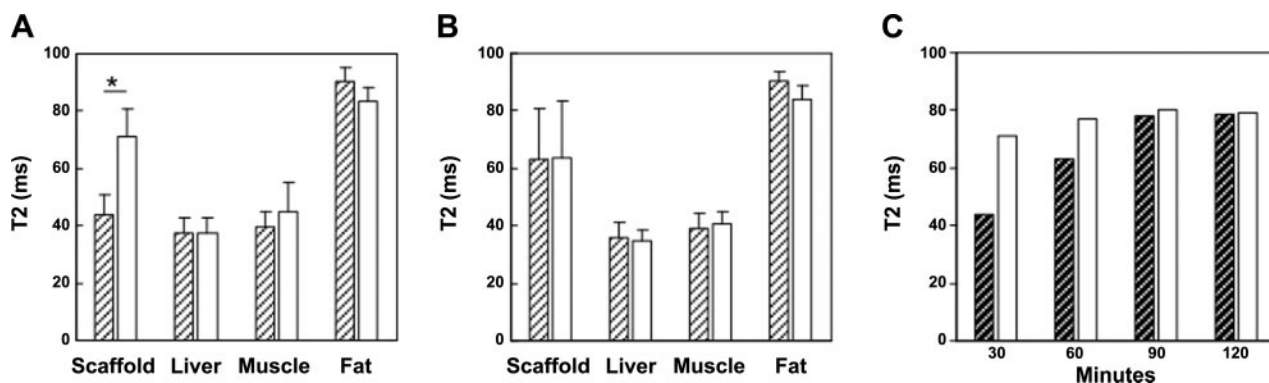


Figure 4. *In vivo* T_2 values for serial MRI of scaffold implants. *A, B*) T_2 values for scaffold implants and extravascular tissues in mice with USPIO-labeled implants (striped bars) and mice with non-USPIO-labeled implants (open bars) imaged immediately after implantation (*A*) and 1 wk postimplantation (*B*). *C*) To gain further insight into the temporal increase in the T_2 value in the labeled scaffolds, T_2 values were calculated for scaffold implants in one additional mouse with a USPIO-labeled implant (striped bars) and one with a non-USPIO-labeled implant (open bars) at 30-min increments starting immediately after implantation.

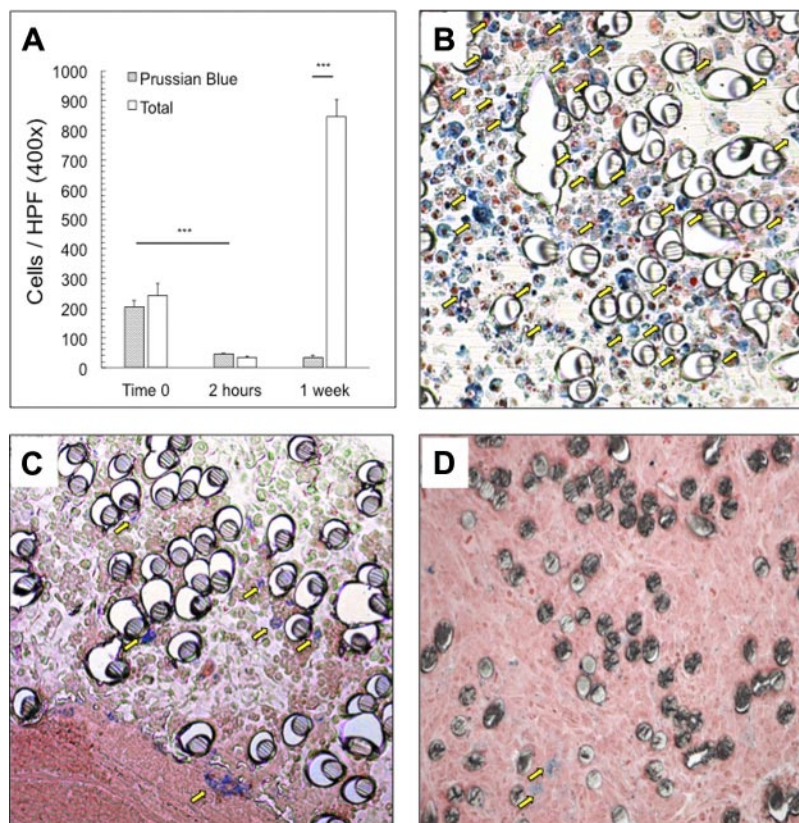
USPIO-labeled cells ($203.625 \pm 21.085/\text{HPF}$, $\times 400$) visible immediately postimplantation ($T=0$) than after 2 h ($45.0 \pm 3.830/\text{HPF}$, $\times 400$) or 1 wk ($34.333 \pm 6.098/\text{HPF}$, $\times 400$). The number of Prussian blue-stained cells was not significantly different after 2 h or 1 wk postimplantation, indicating that the majority of seeded cells were lost from the scaffold immediately after implantation in the animal. In addition, the total number of cells in the scaffold at T_0 and after 2 h was not significantly different from the number of Prussian blue-labeled cells at these time points. However, by 1 wk postimplantation, the total number of cells in the scaffolds was significantly higher than the number of

Prussian blue-labeled cells due to host cell infiltration. These findings support the cellular MR imaging data correlating the rapid increase in T_2 value postimplantation to the rapid loss of seeded cells from the TEVG.

DISCUSSION

To our knowledge, this study is the first application of noninvasive MRI to study the process of neotissue development in a functional tissue-engineered construct with the use of serial imaging in a living animal

Figure 5. Fate of seeded cells by histological analysis. Scaffold explants were stained with Prussian blue to identify intracellular iron deposits. *A*) Number of Prussian blue-labeled cells per HPF (shaded bars) and total number of cells per HPF (open bars) were counted immediately after implantation (time 0), 2 h, and 1 wk after implantation. *B–D*) Representative images of scaffold sections were stained with Prussian blue at time 0 (*B*), 2 h (*C*), and 1 wk (*D*). Arrows indicate macrophages stained with Prussian blue.



model. Prior to this study, there have not been any studies that have used noninvasive cellular MRI to answer questions about cellular-level processes occurring after *in vivo* implantation. Saldanha and colleagues demonstrated the feasibility of single-time-point visualization of iron oxide particle-labeled mesenchymal stem cells (MSCs) in *ex vivo* models of intervertebral disc (33) and bovine osteochondral knee defect (34) repairs. In 2010, Poirier-Quinot *et al.* (35) demonstrated the potential of using MR imaging for visualization of nonfunctional tissue-engineered scaffolds seeded with iron oxide-labeled MSCs before and after subcutaneous implantation in mice. In the field of vascular tissue engineering, Nelson *et al.* (36) used USPIO-labeled cells to enhance visualization of TEVGs postimplantation. We have gone one step further by using noninvasive serial MRI to track the fate of cells used to seed the TEVGs. Our work supports recently published data indicating that the cells used to seed the TEVG preimplantation are not incorporated into the neovessel, as previously thought (37), but are instead rapidly lost from the TEVG postimplantation (39, 40).

To accomplish this, we first optimized USPIO incubation conditions. The RAW 264.7 macrophage/monocyte cell line was utilized for all experiments. This decision was based on the fact that bone marrow mononuclear cells have been used to seed scaffolds in clinical studies since 2001 (41), prior analysis showing that the bone marrow cell population is composed predominantly of monocytes (39), and evidence that monocytes are critical in driving neovessel formation and maintaining graft patency (39, 42). In addition, there is well-established evidence that macrophages are ideal for MRI contrast cell labeling and *in vivo* cell tracking (43–45). Cell labeling was accomplished using USPIO nanoparticles without poly-L-lysine on their surface. The addition of poly-L-lysine to the surface of USPIO particles can enhance cellular uptake, but it also increases the cellular toxicity of the nanoparticles (23). Macrophages and monocytes are traditionally known to robustly engulf MR contrast agents without poly-L-lysine (43, 46), and we achieved adequate cell labeling without poly-L-lysine at a USPIO concentration of 2 mg/ml without affecting cellular metabolic activity or viability. This is consistent with previous investigations in macrophage and monocyte cell lines that have found no significant toxic effects with a labeling concentration as high as 10 mg/ml of USPIO (43).

These labeling conditions provided a reasonable cellular limit of detection between 175,000 and 35,000 cells. This is similar to the detection threshold of $\sim 10^5$ cells that is commonly cited in other literature looking at *in vivo* applications of USPIO cell tracking (17, 47, 48). When the studies are being performed *in vivo*, a major complication is the motion artifact that occurs with the respiratory rate and the heart rate. Under ideal conditions and in organs where motion can almost be completely eliminated, such as in the brain, single-cell detection has become possible (17, 49–51). However, the field is still working toward this becoming a routine capability for use with *in vivo* models of cellular MRI. For our model of vascular tissue engineering and TEVG development, the detection limit is exactly what would

be expected for an *in vivo* application dealing with an active circulating system and respiration.

With this cellular limit of detection and a seeding efficiency of 8%, TEVGs seeded with USPIO-labeled macrophages were easily identified on MRI both *in vitro* and *in vivo*, appearing larger and darker than the TEVGs seeded with unlabeled macrophages, and causing a remarkable decrease in T_2 relaxivity. The USPIO-labeled TEVGs appeared larger due to the blooming effect, an amplification of signal changes produced by microscopic inhomogeneities in the magnetic field that produce a rapid dephasing of diffusing water protons, including those some distance away, leading to a hypointense effect that extends beyond the individual particles (16, 20). Although this can be seen as a disadvantage, in our current application the blooming effect has actually been beneficial in allowing for an increased sensitivity of detection of TEVGs within the native vessel background.

For the *in vivo* application, USPIO-labeled biodegradable scaffolds were implanted as infrarenal interposition grafts in the IVCs of SCID/bg mice. The SCID/bg mouse strain has been well characterized as an adequate model for studying TEVG development, with patency rates approaching 100% in both arterial and venous models (39, 52). All of our TEVG implants remained patent without evidence of stenosis or thrombosis at the time of explantation. T_2 mapping of the IVC scaffold implants showed a drop in T_2 signal intensity immediately after implantation that was no longer observed at 1 wk postimplantation. Serial imaging in 30-min increments revealed the T_2 signal increased to control levels within 90–120 min of implantation. This rapid increase in T_2 signal intensity correlates with the loss of USPIO-labeled cells from the scaffolds, as verified with Prussian blue staining for the presence of iron oxide-labeled cells. The number of iron oxide-labeled cells decreases significantly as early as 2 h postimplantation and is not statistically different from this point to 1 wk postimplantation, leading us to believe that all of the iron oxide-labeled cells are lost from the implanted scaffold by 2 h postimplantation. These data support recently published work (39, 40) showing that the seeded cells are rapidly lost from the TEVG postimplantation and are not detectable in the neovessel. Roh *et al.* (39) tracked the fate of seeded human bone marrow-derived mononuclear cells in our immunodeficient mouse model of TEVG development. Serial postimplantation monitoring with histology and PCR showed that the number of human cells within the TEVGs after 1 wk was below the limit of detection by PCR. Hibino *et al.* (40), tracked the fate of seeded syngeneic bone marrow-derived mononuclear cells labeled with green fluorescent protein (GFP) in an immunocompetent mouse model, which similarly showed the rapid loss of cells by GFP DNA quantification. In both instances, the loss of the seeded cells was accompanied by a rapid infiltration of host monocytes/macrophages and, eventually, by host endothelial and smooth muscle cells. Although both of these works and our present study have clearly shown the rapid loss of the seeded cells, we are still uncertain of the exact mechanism by which this occurs. The cells could be lost

from the implanted TEVG secondary to embolization, apoptosis, or phagocytosis by host macrophages. We think that a form of graft rejection is unlikely because we are using a SCID/bg mouse strain that possesses defective T cells and NK cells. We know that the seeded cells are replaced by infiltrating host macrophages that are not detectable by MRI, and we also hypothesize that embolization is an important mechanism of cell loss in which the cells are washed away from the TEVG after the introduction to the circulation. Determining the exact mechanism of the loss of the seeded cells is an area of future investigation.

The novelty of this study is that it represents a major advancement in the field of tissue engineering by successfully applying noninvasive monitoring to study a cellular-level process. Although we have already demonstrated the rapid loss of the seeded cells from the TEVG in previous works (39, 40), in order to obtain these data, we had to sacrifice animals at each time point to perform tissue analysis. In our present study, we provide additional support for the fate of the seeded cells using noninvasive monitoring with cellular MRI. This is the first time cellular MRI has been successfully applied for real-time serial *in vivo* monitoring in the field of tissue engineering, and our data are in accordance with the results of the previously mentioned invasive approaches.

The paucity of noninvasive techniques currently available to monitor the fate of transplanted tissue-engineered constructs is commonly cited as one of the major challenges facing the translation of regenerative medicine into the clinical realm (35). A noninvasive approach is instrumental for studying the complex process of neotissue development. It is instrumental for the determination of the trafficking and biodistribution of cells *in vivo* after delivery. In addition, it is also important for establishing whether the cells are functioning or have differentiated into the desired cell type, and whether the cells have reached and have remained at their target locations. The information gained from tracking the cells can be used in several important ways: to ensure the appropriate route of delivery, provide feedback about the preferred site of engraftment, and aid in determining the optimal dosing schedule and cell number for achieving desired therapeutic outcomes and ensuring adequate neotissue development (17, 53–55). Classic techniques involving histological analysis provide superior spatial resolution in local microenvironments but are severely limited in their ability to resolve dynamic changes. Previously applied noninvasive techniques, such as intravital fluorescence microscopy, which has been used to track fluorescently labeled cells in tissue (13), are not ideal for routine investigations with our TEVGs because of their ability to image only superficial or explanted tissue (56). These data are very promising with respect to the use of cellular MRI in tissue engineering as the preferred method of noninvasive cellular monitoring.

However, there are still several limitations associated with the use of USPIO particles for cell tracking and the currently available MRI technology. One major limitation is the fact that iron oxide is a T_2 contrast agent that creates a hypointense (dark) signal. This signal may be

confounded with similar hypointense MR signals originating from the vasculature, hemorrhages, or tumors (25). In addition, void detection is dependent on image resolution, a parameter limited by partial volume effects (55). These drawbacks are being overcome by the trend of producing agents with lower thresholds of detectability, the installation of scanners with higher field strengths (23), and a focus on imaging the off-resonance effects (17). A final solution to this problem involves the development of gadolinium-based nanoparticulate contrast agents that have better cell toxicity profiles (57).

Another confounding factor is the possibility that the loss of MR signal could be caused by dilution of the contrast agent through cell division or biodegradation instead of dispersion of cells carrying the label (36). However, many research groups have shown that although the iron load is diluted with cell division, the signal is still strong enough to be detected for ≥ 7 d and even longer depending on the rate of cell division and initial iron load (26, 35, 36). In our work, it is possible that the increase in T_2 signal was caused by the rapid exocytosis or metabolism of the iron oxide particles. However, this is unlikely due to the time frame with which the signal increased and previously reported evidence that macrophages are able to retain endocytosed iron oxide particles in large enough quantities to produce a drop in MR signal intensity for ≥ 10 d postlabeling (43). Terrovitis *et al.* (31) demonstrated ferumoxide labeling that remained effective on scans up to 4 wk after the labeling procedure.

One major limitation with bringing this technology into the clinical realm is the current lack of interest in MR-compatible device development (17). MRI has not yet become a part of standard laboratory equipment. This is mostly due to the large investment that goes into maintaining a superconducting MRI device, as well as the lack of development of specially designed coils and other equipment necessary to image samples of multiple sizes and shapes (58). In addition, the most widely used strategy for increasing the spatial resolution (a requirement for cell tracking application) requires the use of high-field MRI to increase the signal-to-noise ratio in a voxel by enhancing the magnetic field strength. However, high-field MRI is not currently available in the clinical setting and has several limitations, such as high cost, reduced bore size, and artifact susceptibility.

Although there are still significant limitations with this technology, more groups are realizing the importance of using noninvasive techniques to study the dynamic changes that occur as their tissue-engineered constructs develop. In our research group, we are already performing additional cell-tracking studies. From previous reports, we know that after the seeded cells are lost from the implanted TEVG, there is a rapid infiltration of host macrophages that initiate an inflammatory process of vascular remodeling (39, 40). The next phase of this research will involve using cellular MRI to track the infiltration of host inflammatory cells into implanted TEVGs.

With the development of more sensitive MR contrast agents and with increased access to more advanced MR

technology, noninvasive cellular MRI will become an integral part of vascular tissue engineering. Knowledge gained through this research will be instrumental in creating improved TEVGs, for directing neovessel development, and for use in the clinical setting as a valuable monitoring technique to improve patient outcomes. EJ

Research support was provided through the Howard Hughes Medical Institute, the Yale University Department of Surgery Ohse Grant Program, the Yale University Office of Student Research, and the U.S. National Institutes of Health (NIH; grants UL1RR024139, R01-HL098228, and K08HL083980). This work was performed as part of an NIH-sponsored Howard Hughes Medical Institute Medical Research Training Fellowship. Gunze Ltd. has provided research support for the clinical trial evaluating the use of tissue-engineered vascular grafts. None of the funding for the work done in this manuscript was provided by Gunze Ltd.

REFERENCES

- Kim, S.-J., Kim, W.-H., Lim, H.-G., and Lee, J.-Y. (2008) Outcome of 200 patients after an extracardiac Fontan procedure. *J. Thoracic Cardiovasc. Surg.* **136**, 108–116
- Gentles, T. L., Gauvreau, K., Mayer, J. E., Fishberger, S. B., Burnett, J., Colan, S. D., Newburger, J. W., and Wernovsky, G. (1997) Functional outcome after the Fontan operation: factors influencing late morbidity. *J. Thorac. Cardiovasc. Surg.* **114**, 392–403
- Hibino, N., McGillicuddy, E., Matsumura, G., Ichihara, Y., Naito, Y., Breuer, C., and Shin'oka, T. (2010) Late-term results of tissue-engineered vascular grafts in humans. *J. Thorac. Cardiovasc. Surg.* **139**, 431–436
- Shin'oka, T., Matsumura, G., Hibino, N., Naito, Y., Watanabe, M., Konuma, T., Sakamoto, T., Nagatsu, M., and Kurosawa, H. (2005) Midterm clinical result of tissue-engineered vascular autografts seeded with autologous bone marrow cells. *J. Thorac. Cardiovasc. Surg.* **129**, 1330–1338
- Roh, J. D., Nelson, G. N., Brennan, M. P., Mirensky, T. L., Yi, T., Hazlett, T. F., Tellides, G., Sinusas, A. J., Pober, J. S., Saltzman, W. M., Kyriakides, T. R., and Breuer, C. K. (2008) Small-diameter biodegradable scaffolds for functional vascular tissue engineering in the mouse model. *Biomaterials* **29**, 1454–1463
- Lopez-Soler, R. L., Brennan, M. P., Goyal, A., Wang, Y., Fong, P., Tellides, G., Sinusas, A., Dardik, A., and Breuer, C. (2007) Development of a mouse model for evaluation of small diameter vascular grafts. *J. Surg. Res.* **139**, 1–6
- Watanabe, M., Shin'oka, T., Tohyama, S., Hibino, N., Konuma, T., Matsumura, G., Kosaka, Y., Ishida, T., Imai, Y., Yamakawa, M., Ikada, Y., and Morita, S. (2001) Tissue-engineered vascular autograft: inferior vena cava replacement in a dog model. *Tissue Eng.* **7**, 429–439
- Matsumura, G., Ishihara, Y., Miyagawa-Tomita, S., Ikada, Y., Matsuda, S., Kurosawa, H., and Shin'oka, T. (2006) Evaluation of tissue-engineered vascular autografts. *Tissue Eng.* **12**, 3075–3083
- Brennan, M. P., Dardik, A., Hibino, N., Roh, J. D., Nelson, G. N., Papademitris, X., Shin'oka, T., and Breuer, C. K. (2008) Tissue-engineered vascular grafts demonstrate evidence of growth and development when implanted in a juvenile animal model. *Trans. Mtg. Am. Surg. Assoc.* **126**, 20–27
- Giannico, S., Hammad, F., Amodeo, A., Michielon, G., Drago, F., Turchetta, A., Di, Donato, R., and Sanders, S. P. (2006) Clinical outcome of 193 extracardiac Fontan patients: the first 15 years. *J. Am. Coll. Cardiol.* **47**, 2065–2073
- Samánek, M. (1992) Children with congenital heart disease: probability of natural survival. *Pediatr. Cardiol.* **13**, 152–158
- Yamanami, M., Yamamoto, A., Iida, H., Watanabe, T., Kanda, K., Yaku, H., and Nakayama, Y. (2010) 3-Tesla magnetic resonance angiographic assessment of a tissue-engineered small-caliber vascular graft implanted in a rat. *J. Biomed. Mater. Res.* **92B**, 156–160
- Hjortnaes, J., Gottlieb, D., Figueiredo, J.-L., Melero-Martin, J., Kohler, R. H., Bischoff, J., Weissleder, R., Mayer, J. E., and Aikawa, E. (2010) Intravital molecular imaging of small-diameter tissue-engineered vascular grafts in mice: a feasibility study. *Tissue Eng. Part C. Methods* **16**, 597–607
- Burtea, C., Laurent, S., Mahieu, I., Larbanoix, L., Roch, A., Port, M., Rousseaux, O., Ballet, S., Murariu, O., Toubeau, G., Corot, C., Vander Elst, L., and Muller, R. N. (2010) In vitro biomedical applications of functionalized iron oxide nanoparticles, including those not related to magnetic properties. [E-pub ahead of print] *Contrast Media Mol. Imaging* doi: 10.1002/cmmi.423
- Burtea, C., Laurent, S., Vander, Elst, L., and Muller, R. N. (2008) Contrast agents: magnetic resonance. *Handb. Exp. Pharmacol.* **185**, 135–165
- Bulte, J. W. M., Duncan, I. D., and Frank, J. A. (2002) In vivo magnetic resonance tracking of magnetically labeled cells after transplantation. *J. Cereb. Blood Flow Metab.* **22**, 899–907
- Kraitchman, D. L., Gilson, W. D., and Lorenz, C. H. (2008) Stem cell therapy: MRI guidance and monitoring. *J. Magn. Reson. Imaging* **27**, 299–310
- De Vries, I. J. M., Lesterhuis, W. J., Barentsz, J. O., Verdijk, P., van Krieken, J. H., Boerman, O. C., Oyen, W. J., Bonenkamp, J. J., Boezeman, J. B., Adema, G. J., Bulte, J. W., Scheenen, T. W., Punt, C. J., Heerschap, A., and Figdor, C. G. (2005) Magnetic resonance tracking of dendritic cells in melanoma patients for monitoring of cellular therapy. *Nat. Biotechnol.* **23**, 1407–1413
- Crich, S. G., Biancone, L., Cantaluppi, V., Duo, D., Esposito, G., Russo, S., Camussi, G., and Aime, S. (2004) Improved route for the visualization of stem cells labeled with a Gd-/Eu-Chelate as dual (MRI and fluorescence) agent. *Magn. Reson. Med.* **51**, 938–944
- Rogers, W. J., Meyer, C. H., and Kramer, C. M. (2006) Technology insight: in vivo cell tracking by use of MRI. *Nat. Clin. Pract. Cardiovasc. Med.* **3**, 554–562
- Rogers, W. J., Meyer, C. H., and Kramer, C. M. (2006) Technology insight: in vivo cell tracking by use of MRI. *Nat. Clin. Pract. Cardiovasc. Med.* **3**, 554–562
- Shapiro, E. M., Medford-Davis, L. N., Fahmy, T. M., Dunbar, C. E., and Koretsky, A. P. (2007) Antibody-mediated cell labeling of peripheral T cells with micron-sized iron oxide particles (MPIOs) allows single cell detection by MRI. *Contrast Media Mol. Imaging* **2**, 147–153
- Bulte, J. W. M., and Kraitchman, D. L. (2004) Iron oxide MR contrast agents for molecular and cellular imaging. *NMR Biomed.* **17**, 484–499
- Heyn, C., Bowen, C. V., Rutt, B. K., and Foster, P. J. (2005) Detection threshold of single SPIO-labeled cells with FIESTA. *Magn. Reson. Med.* **53**, 312–320
- Kubínová, Š., and Syková, E. (2010) Nanotechnologies in regenerative medicine. *Minim. Inv. Ther. Allied Technol.* **19**, 144–156
- Strijkers, G. J., Mulder, W. J. M., van Tilborg, G. A. F., and Nicolay, K. (2007) MRI contrast agents: current status and future perspectives. *Anticancer Agents Med. Chem.* **7**, 291–305
- Perea, H., Aigner, J., Heverhagen, J. T., Hopfner, U., and Wintermantel, E. (2007) Vascular tissue engineering with magnetic nanoparticles: seeing deeper. *J. Tissue Eng. Regen. Med.* **1**, 318–321
- Shimizu, K., Ito, A., Arinobe, M., Murase, Y., Iwata, Y., Narita, Y., Kagami, H., Ueda, M., and Honda, H. (2007) Effective cell-seeding technique using magnetite nanoparticles and magnetic force onto decellularized blood vessels for vascular tissue engineering. *J. Biosci. Bioeng.* **103**, 472–478
- Ito, A., Ino, K., Hayashida, M., Kobayashi, T., Matsumura, H., Kagami, H., Ueda, M., and Honda, H. (2005) Novel methodology for fabrication of tissue-engineered tubular constructs using magnetite nanoparticles and magnetic force. *Tissue Eng.* **11**, 1553–1561
- Villalona, G. A., Udelsman, B., Duncan, D. R., McGillicuddy, E., Sawh-Martinez, R. F., Hibino, N., Painter, C., Mirensky, T., Erickson, B., Shin'oka, T., and Breuer, C. K. (2010) Cell-seeding techniques in vascular tissue engineering. *Tissue Eng. B. Rev.* **16**, 341–350
- Terrovitis, J. V., Bulte, J. W. M., Sarvananthan, S., Crowe, L. A., Sarathchandra, P., Batten, P., Sachlos, E., Chester, A. H., Czernuszka, J. T., Firmin, D. N., Taylor, P. M., and Yacoub, M. S. (2008) In vivo MRI tracking of stem cells seeded into a rat heart. *J. Magn. Reson. Imaging* **28**, 103–110

- M. H. (2006) Magnetic resonance imaging of ferumoxide-labeled mesenchymal stem cells seeded on collagen scaffolds? Relevance to tissue engineering. *Tissue Eng.* **12**, 2765–2775
32. Heymer, A., Haddad, D., Weber, M., Gbureck, U., Jakob, P. M., Eulert, J., and Nöth U. (2008) Iron oxide labelling of human mesenchymal stem cells in collagen hydrogels for articular cartilage repair. *Biomaterials* **29**, 1473–1483
 33. Saldanha, K. J., Piper, S. L., Ainslie, K. M., Kim, H. T., and Majumdar, S. (2008) Magnetic resonance imaging of iron oxide labelled stem cells: applications to tissue engineering based regeneration of the intervertebral disc. *Eur. Cell. Mater.* **16**, 17–25
 34. Saldanha, K. J., Doan, R. P., Ainslie, K. M., Desai, T. A., and Majumdar, S. (2011) Micrometer-sized iron oxide particle labeling of mesenchymal stem cells for magnetic resonance imaging-based monitoring of cartilage tissue engineering. *Magn. Reson. Imaging* **29**, 40–49
 35. Poirier-Quinot, M., Frasca, G., Wilhelm, C., Luciani, N., Ginefri, J.-C., Darrasse, L., Letourneur, D., Le Visage, C., and Gazeau, F. (2010) High-resolution 1.5-Tesla magnetic resonance imaging for tissue-engineered constructs: a noninvasive tool to assess three-dimensional scaffold architecture and cell seeding. *Tissue Eng. C Methods* **16**, 185–200
 36. Nelson, G. N., Roh, J. D., Mirensky, T. L., Wang, Y., Yi, T., Tellides, G., Pober, J. S., Shkarin, P., Shapiro, E. M., Saltzman, W. M., Papademetris, X., Fahmy, T. M., and Breuer, C. K. (2008) Initial evaluation of the use of USPIO cell labeling and noninvasive MR monitoring of human tissue-engineered vascular grafts in vivo. *FASEB J.* **22**, 3888–3895
 37. Matsumura, G., Miyagawa-Tomita, S., Shin'oka, T., Ikada, Y., and Kurosawa, H. (2003) First evidence that bone marrow cells contribute to the construction of tissue-engineered vascular autografts in vivo. *Circulation* **108**, 1729–1734
 38. Noishiki, Y., Tomizawa, Y., Yamane, Y., and Matsumoto, A. (1996) Autocrine angiogenic vascular prosthesis with bone marrow transplantation. *Nat. Med.* **2**, 90–93
 39. Roh, J. D., Sawh-Martinez, R., Brennan, M. P., Jay, S. M., Devine, L., Rao, D. A., Yi, T., Mirensky, T. L., Nalbandian, A., Udelsman, B., Hibino, N., Shinoka, T., Saltzman, W. M., Snyder, E., Kyriakides, T. R., Pober, J. S., and Breuer, C. K. (2010) Tissue-engineered vascular grafts transform into mature blood vessels via an inflammation-mediated process of vascular remodeling. *Proc. Natl. Acad. Sci. USA* **107**, 4669–4674
 40. Hibino, N., Villalona, G., Pietris, N., Duncan, D. R., Schoffner, A., Roh, J. D., Yi, T., Dobrucki, L. W., Mejias, D., Sawh-Martinez, R., Harrington, J. K., Sinusas, A., Krause, D. S., Kyriakides, T., Saltzman, W. M., Pober, J. S., Shin'oka, T., and Breuer, C. K. (2011) Tissue-engineered vascular grafts form neovessels that arise from regeneration of the adjacent blood vessel. *FASEB J.* **25**, 2731–2739
 41. Matsumura, G., Hibino, N., Ikada, Y., Kurosawa, H., and Shin'oka, T. (2003) Successful application of tissue engineered vascular autografts: clinical experience. *Biomaterials* **24**, 2303–2308
 42. Mirensky, T. L., Hibino, N., Sawh-Martinez, R. F., Yi, T., Villalona, G., Shinoka, T., and Breuer, C. K. (2010) Tissue-engineered vascular grafts: does cell seeding matter? *J. Ped. Surg.* **45**, 1299–1305
 43. Müller, K., Skepper, J. N., Posfai, M., Trivedi, R., Howarth, S., Corot, C., Lancelot, E., Thompson, P. W., Brown, A. P., and Gillard, J. H. (2007) Effect of ultrasmall superparamagnetic iron oxide nanoparticles (ferumoxtran-10) on human monocyte-macrophages in vitro. *Biomaterials* **28**, 1629–1642
 44. Metz, S., Bonaterra, G., Rudelius, M., Settles, M., Rummeny, E. J., and Daldrup-Link, H. E. (2004) Capacity of human monocytes to phagocytose approved iron oxide MR contrast agents in vitro. *Eur. Radiol.* **14**, 1851–1858
 45. Anzai, Y., and Prince, M. R. Iron oxide-enhanced MR lymphography: the evaluation of cervical lymph node metastases in head and neck cancer (1997). *J. Magn. Reson. Imaging* **7**, 75–81
 46. Trivedi, R. A., U-King-Im, J.-M., Graves, M. J., Cross, J. J., Horsley, J., Goddard, M. J., Skepper, J. N., Quartey, G., Warburton, E., Joubert, I., Wang, L., Kirkpatrick, P. J., Brown, J., and Gillard, J. H. (2004) In vivo detection of macrophages in human carotid atheroma: temporal dependence of ultrasmall superparamagnetic particles of iron oxide-enhanced MRI. *Stroke* **35**, 1631–1635
 47. Bulte, J. W. M., and Kraitchman, D. L. (2004) Monitoring cell therapy using iron oxide MR contrast agents. *Curr. Pharm. Biotechnol.* **5**, 567–584
 48. Hill, J. M., Dick, A. J., Raman, V. K., Thompson, R. B., Yu, Z.-X., Hinds, K. A., Pessanha, B. S., Guttman, M. A., Varney, T. R., Martin, B. J., Dunbar, C. E., McVeigh, E. R., and Lederman, R. J. (2003) Serial cardiac magnetic resonance imaging of injected mesenchymal stem cells. *Circulation* **108**, 1009–1014
 49. Foster-Gareau, P., Heyn, C., Alejski, A., and Rutt, B. K. (2003) Imaging single mammalian cells with a 1.5 T clinical MRI scanner. *Magn. Reson. Med.* **49**, 968–971
 50. Zhang, Z., van den Bos, E. J., Wielopolski, P. A., de Jong-Popijus, M., Duncker, D. J., and Krestin, G. P. (2004) High-resolution magnetic resonance imaging of iron-labeled myoblasts using a standard 1.5-T clinical scanner. *MAGMA* **17**, 201–209
 51. Shapiro, E. M., Sharer, K., Skrtic, S., and Koretsky, A. P. (2006) In vivo detection of single cells by MRI. *Magn. Reson. Med.* **55**, 242–249
 52. Nelson, G. N., Mirensky, T., Brennan, M. P., Roh, J. D., Yi, T., Wang, Y., and Breuer, C. K. (2008) Functional small-diameter human tissue-engineered arterial grafts in an immunodeficient mouse model: preliminary findings. *Arch. Surg.* **143**, 488–494
 53. Arbab, A. S., and Frank, J. A. (2008) Cellular MRI and its role in stem cell therapy. *Regen. Med.* **3**, 199–215
 54. Feigenbaum, G. S., Lemberg, L., and Hare, J. M. (2009) Tracking cell fate with noninvasive imaging. *J. Am. Coll. Cardiol.* **54**, 1627–1628
 55. Liu, W., and Frank, J. A. (2009) Detection and quantification of magnetically labeled cells by cellular MRI. *Eur. J. Radiol.* **70**, 258–264
 56. Miller, M. J., Wei, S. H., Cahalan, M. D., and Parker, I. (2003) Autonomous T cell trafficking examined in vivo with intravital two-photon microscopy. *Proc. Natl. Acad. Sci. U. S. A.* **100**, 2604–2609
 57. Mohs, A. M., and Lu, Z.-R. (2007) Gadolinium(III)-based blood-pool contrast agents for magnetic resonance imaging: status and clinical potential. *Expert Opin. Drug Deliv.* **4**, 149–164
 58. Nitzsche, H., Metz, H., Lochmann, A., Bernstein, A., Hause, G., Groth, T., and Mäder, K. (2009) Characterization of scaffolds for tissue engineering by benchtop-magnetic resonance imaging. *Tissue Eng. C Methods* **15**, 513–521

Received for publication March 28, 2011.

Accepted for publication August 4, 2011.